Probabilistic Robustness Analysis of Drag-Free Attitude Control System using Polynomial Chaos

Mario Izquierdo Serra*, Maurice Martin†, Simon Delchambre‡, Stefan Winkler§
Airbus Defence and Space GmbH, Immenstaad am Bodensee, 88090, Germany

Harald Pfifer¶
Technische Universität Dresden, Dresden, 01307, Germany

I. Introduction

The Laser Interferometer Space Antenna (LISA) mission will be the first space-based gravitational wave observatory, consisting of three identical spacecraft (S/C) flying in a triangular formation behind the Earth [1]. Each S/C will sit in a heliocentric orbit at around 50 million km from Earth, with a distance of around 2.5 million km between each S/C [2]. The Drag-Free Attitude Control System (DFACS) is a vital subsystem on board and a key technology in LISA, whose main function is to control the spacecraft dynamics through attitude and translational control [3, 4]. Before nominal science operations, an acquisition sequence needs to be performed to establish the bi-directional laser links between the three spacecraft [5]. This sequence involves several scanning maneuvers, during which DFACS controls the spacecraft dynamics, reducing the risk of missing the other spacecraft and failing to acquire the laser links. DFACS system performance during acquisition has to be guaranteed in presence of a large class of disturbances and uncertain parameters.

This paper presents a probabilistic verification approach for the DFACS acquisition sequence based on Polynomial Chaos Expansion (PCE) and Linear Fractional Transformation (LFT). This article extends the preliminary work in [6] and aims to accelerate the current verification and validation (V&V) processes in industry. Real-world missions typically feature models with many states and uncertainties, which pose significant challenges to the direct application of alternative V&V techniques developed in recent decades [7]. This paper uses a high-fidelity DFACS benchmark to demonstrate the feasibility of this LFT-based PCE approach for industrial application in a challenging real-world mission.

Current and future space missions require increasingly more complex control system designs to achieve more ambitious mission goals. Although the design of these solutions is demanding, assessing the robustness of the system through the V&V process takes up the majority of the overall development time and costs [8]. The default method

*Doctoral Candidate, AOCS/GNC & Flight Dynamics Studies and Mission Analysis, mario.izquierdo_serra@airbus.com; registered as a Dr.-Ing. candidate at the Technische Universität Dresden.

†AOCS/GNC Design and Analysis Engineer, AOCS/GNC & Flight Dynamics Studies and Mission Analysis, maurice.martin@airbus.com

‡AOCS/DFACS Architect, Avionics Delivery and Improvements, simon.delchambre@airbus.com

§Honorary Professor, Senior Expert: Spacecraft Autonomy, Navigation & Control, AOCS/GNC & Flight Dynamics, stefan.st.winkler@airbus.com

¶Professor, Chair of Flight Mechanics and Control, harald.pfifer@tu-dresden.de

used in industry for V&V are Monte Carlo (MC) simulation campaigns [9–11], which currently drive most of the development time in real missions. Overall, it is a time-consuming method, motivating the need to explore alternative V&V methods for complex systems.

Within the robust control framework, some worst-case analysis tools have reached a good level of maturity in space applications. In general, these robustness-based methods (e.g., μ-analysis [12–14], integral quadratic constraint [15, 16]) conduct stability and performance worst-case analysis of systems over an infinite time horizon. More recently, the integral quadratic constraint framework has been extended to finite time horizons [17] and successfully applied on complex aerospace applications [18, 19].

However, this paper focuses on probabilistic performance, since it is often more relevant in the industrial verification process compared to worst-case analysis. The scope of μ-analysis has been extended to include probabilistic stability and performance problems [20]. Still, the finite time horizon of the acquisition sequence is not captured by these extensions. Although the development of more efficient probabilistic V&V methods for finite time horizon systems has received little attention, alternatives based on polynomial chaos have recently been developed [21].

Polynomial chaos is a series expansion (similar to the Fourier series for periodic time signals) that relies on approximating an uncertain system response by fitting orthogonal polynomials to the actual system response [22, 23]. Polynomial chaos was originally introduced in [24] to represent Gaussian processes. Later, PCE was combined in [25] with finite element method in an intrusive way to model solid mechanics uncertainty. PCE was also generalized in [26, 27] to non-Gaussian random inputs through a family of orthogonal polynomials known as Askey scheme. For uncertain dynamic systems depending on random parameters, the common approach is to project the differential equations on a polynomial orthogonal basis of the random parameters. This is commonly referred to as intrusive Galerkin projection and offers superior convergence to other methods (e.g., Monte Carlo) when the regularity (i.e., smoothness) of the function to approximate is sufficient and the dimension is not too high. However, conventional Galerkin projection alters the differential equations in a critical way that does not preserve important system properties (e.g., stability). In [28] it is shown that using an LFT, and projecting the LFT instead of the original system preserves important system characteristics. In addition, [29] highlights that the computation of PCE on LFTs becomes much more efficient. Both of these results have been successfully applied to an auto-landing system of a civil transport aircraft in [30]. This paper uses an LFT-based PCE on a more complex system, with the objective of efficiently analyzing the influence of uncertainties on DFACS performance during the scanning phase of the acquisition sequence.

II. Background

A. Uncertain Stochastic Systems

Consider a linear system defined on $t \in [0, T]$ with finite time horizon $T < \infty$ subject to stochastic uncertain parameters δ of the following form:

$$\begin{aligned} \dot{x}(t,\delta) &= A(\delta)x(t,\delta) + B(\delta)u(t) \\ y(t,\delta) &= C(\delta)x(t,\delta) + D(\delta)u(t). \end{aligned} \tag{1}$$

Here, $x(t,\delta) \in \mathbb{R}^{n_x}$ is the state vector, $u(t) \in \mathbb{R}^{n_u}$ the input vector, and $y(t,\delta) \in \mathbb{R}^{n_y}$ the output vector. Moreover, $\delta \in \Delta^{n_\delta}$ is an unknown time-invariant parameter vector bounded within a suitable compact set $\Delta^{n_\delta} \subset \mathbb{R}^{n_\delta}$, subject to a given probability distribution $p(\delta)$, where n_δ represents the number of uncertain parameters. A, B, C, and D are matrix functions, independent of time, that map each δ to a matrix of appropriate dimension. It is often of interest to estimate the probability distribution function of the output $y(t,\delta)$ subject to a given input $u(t)$ and an uncertainty set Δ^{n_δ} with an input probability distribution $p(\delta)$.

B. Linear Fractional Transformation

Linear Fractional Transformation is a general, powerful and flexible way to represent uncertainty in systems [31]. Consider the uncertain system in Eq. (1). Assuming the state-space matrices A, B, C, and D depend rationally on δ, the general system in Eq. (1) can be transformed into the interconnection of a deterministic system M:

$$\begin{bmatrix} \dot{x}(t,\delta) \\ v(t,\delta) \\ y(t,\delta) \end{bmatrix} = \begin{bmatrix} A_M & B_w & B_u \\ C_v & D_{vw} & D_{vu} \\ C_y & D_{yw} & D_{yu} \end{bmatrix} \begin{bmatrix} x(t,\delta) \\ w(t,\delta) \\ u(t) \end{bmatrix} \tag{2}$$

with an isolated uncertain part

$$w(t,\delta) = \Delta(\delta)v(t,\delta), \tag{3}$$

where Δ depends linearly on δ. Given that only parametric uncertainties are considered in this paper, Δ is a diagonal matrix of the form $\Delta(\delta) = \mathrm{diag}(\delta_1 I_{m_1}, \ldots, \delta_{n_\delta} I_{m_{n_\delta}})$, where δ_i represents the (i)-th entry of the unknown parameter vector δ, m_i the multiplicity of uncertainty δ_i, and I_{m_i} the identity matrix of order m_i. LFT-based uncertainty descriptions separate what is known (nominal) from what is unknown (uncertain) as shown in Fig. 1.

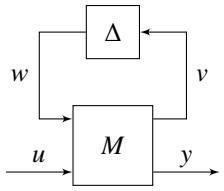

Fig. 1 Linear Fractional Transformation. M is the nominal part, and Δ the uncertainty.

C. Polynomial Chaos Series Expansion

Polynomial chaos is an orthogonal series expansion used in the field of uncertainty quantification [22]. The key idea behind PCE is to express the output of the system in Eq. (1) using appropriate orthogonal basis polynomials $\psi_\alpha : \Delta^{n_\delta} \to \mathbb{R}$:

$$y(t,\delta) = \sum_{\alpha=0}^{\infty} y_\alpha(t)\psi_\alpha(\delta). \tag{4}$$

Therein, $\alpha \in \mathbb{N}_0$, the y_α are time-variant deterministic expansion coefficients, and ψ_α are the orthogonal polynomials of degree α with respect to the probability density function of δ. Some polynomial families (e.g., Legendre, Hermite, Jacobi, etc.) are orthogonal with respect to some continuous probability density functions (e.g., uniform, Gaussian/normal, beta, etc.) [32]. In this context, orthogonality is defined as:

$$\begin{aligned} \psi_0 &= 1 \\ \langle \psi_\alpha, \psi_\beta \rangle &= \begin{cases} 0 & \text{if } \alpha \neq \beta \\ \mathbb{E}[\psi_\alpha^2] & \text{if } \alpha = \beta \end{cases} \qquad \forall \alpha, \beta \in \mathbb{N}_0, \end{aligned} \tag{5}$$

where $\langle \cdot, \cdot \rangle$ denotes the inner product:

$$\langle f, g \rangle = \mathbb{E}[fg] = \int_{\Delta^{n_\delta}} f(\delta)g(\delta)p(\delta)d\delta, \tag{6}$$

defined via the expectation $\mathbb{E}[\cdot]$ w.r.t. the probability density function $p(\delta)$.

The y_α coefficients, often called stochastic modes, are defined through the projection relation:

$$y_\alpha = \frac{\langle y(t,\cdot), \psi_\alpha \rangle}{\langle \psi_\alpha, \psi_\alpha \rangle} = \frac{\mathbb{E}[y(t,\delta)\psi_\alpha]}{\mathbb{E}[\psi_\alpha^2]} = \frac{\int_{\Delta^{n_\delta}} y(t,\delta)\psi_\alpha(\delta)p(\delta)d\delta}{\int_{\Delta^{n_\delta}} \psi_\alpha^2(\delta)p(\delta)d\delta}. \tag{7}$$

In practice, the infinite series in Eq. (4) needs to be truncated (see, e.g., [33]) as:

$$y(t,\delta) \approx \sum_{\alpha=0}^{L-1} y_\alpha(t)\psi_\alpha(\delta), \tag{8}$$

where the factor L represents the number of expansion coefficients and, for the total polynomial degree truncation

scheme, is given by:

$$L = \frac{(n_\delta + d)!}{n_\delta! d!}, \tag{9}$$

where d denotes the maximum total polynomial degree. An anisotropic PCE scheme [34] could be very beneficial for a large number of uncertainties, though it was not necessary for this application.

There exist several methods to compute the deterministic expansion coefficients y_α in Eq. (7), which, in general, are often computationally expensive. One particular efficient way is presented in the next Section and will be used in this paper.

D. LFT-based Polynomial Chaos Series Expansion

The polynomial chaos series expansion of uncertain systems in linear fractional representation can offer computational advantages and is briefly presented in this section. For a full mathematical description, see [29]. The main idea is to apply the PCE of Sec. II.C to the system in LFT form (Eq. (2) and Eq. (3)) and employ a Galerkin projection to compute the expansion coefficients. Denote by $\Psi = [\psi_0, ..., \psi_{L-1}]^\top$ the vector concatenating the L polynomial basis functions and by $e_1 = [1, 0, ..., 0]^\top$ the L-dimensional unit vector. Then, the PCE of Eq. (2) is M_Π:

$$\begin{bmatrix} \dot{X}(t) \\ V(t) \\ Y(t) \end{bmatrix} = \begin{bmatrix} A_M \otimes I_L & B_w \otimes I_L & B_u \otimes e_1 \\ C_v \otimes I_L & D_{vw} \otimes I_L & D_{vu} \otimes e_1 \\ C_y \otimes I_L & D_{yw} \otimes I_L & D_{yu} \otimes e_1 \end{bmatrix} \begin{bmatrix} X(t) \\ W(t) \\ u(t) \end{bmatrix}, \tag{10}$$

and the PCE Eq. (3) is:

$$W(t) = \underbrace{(I_{n_\Delta} \otimes \langle \Psi\Psi^\top \rangle)^{-1} \langle \Delta(\delta) \otimes (\Psi\Psi^\top) \rangle}_{=:\Delta_\Pi} V(t). \tag{11}$$

The projection of the matrix Δ is denoted by $\Delta_\Pi \in \mathbb{R}^{(n_\Delta L)\times(n_\Delta L)}$. Moreover, capital vectors $X(t) \in \mathbb{R}^{n_x L}$, $Y(t) \in \mathbb{R}^{n_y L}$, $W(t) \in \mathbb{R}^{n_\Delta L}$, and $V(t) \in \mathbb{R}^{n_\Delta L}$ concatenate the expansion coefficients (Eq. (7)) of the corresponding lower-case vectors $x(t, \delta)$, $y(t, \delta)$, $w(t, \delta)$, and $v(t, \delta)$:

$$\begin{aligned} X(t) &= (I_{n_x} \otimes \langle \Psi\Psi^\top \rangle)^{-1} \langle x(t, \cdot) \otimes \Psi \rangle \\ Y(t) &= (I_{n_y} \otimes \langle \Psi\Psi^\top \rangle)^{-1} \langle y(t, \cdot) \otimes \Psi \rangle \\ W(t) &= (I_{n_\Delta} \otimes \langle \Psi\Psi^\top \rangle)^{-1} \langle w(t, \cdot) \otimes \Psi \rangle \\ V(t) &= (I_{n_\Delta} \otimes \langle \Psi\Psi^\top \rangle)^{-1} \langle v(t, \cdot) \otimes \Psi \rangle. \end{aligned} \tag{12}$$

By closing the upper LFT of Eq. (10) and Eq. (11), and solving the expanded system for $Y(t)$ (which concatenates the expansion coefficients y_α), the output of the system $y(t, \delta)$ can be reconstructed making use of Eq. (8).

The Galerkin projection method maintains the formal mathematical structure of the considered uncertain model (i.e., the expansion of the LFT in Eq. (2) and Eq. (3) remains an LFT in Eq. (10) and Eq. (11)). It generates a system of enhanced dimension, i.e., enlarged by the factor L. According to Eq. (9), the number of expansion terms and, thus, the dimension of the coupled system, increases considerably with the number of uncertainties and the maximum total polynomial degree. For example, for 25 uncertain parameters (i.e., $n_\delta = 25$) and a second order expansion (i.e., $d = 2$), the system's size is enlarged by a factor of $L = 351$. Therefore, in many practical problems very high dimensional systems have to be solved. A detailed analysis of the computational advantages of using an LFT before the Galerkin projection is provided in [29].

III. DFACS Acquisition Problem Description

A. Scanning Phase Tracking Problem

Prior to nominal science operations in LISA, an acquisition sequence is performed to establish the bi-directional laser links between the three spacecraft. At the beginning of the acquisition sequence, one spacecraft scans the expected region of the other spacecraft. During this phase, the DFACS controls the spacecraft attitude to follow the scanning maneuver commanded by the guidance algorithm. Disturbances and uncertainties cause the spacecraft true attitude not to match exactly the reference (or commanded) attitude. Performance requirements are set on this tracking error, to ensure that the deviations from the predefined trajectory stay within certain bounds, and on some system states, that must stay within operational ranges.

Each LISA spacecraft is equipped with a platform, two free-flying test masses and two Moving Optical Sub-Assemblies (MOSAs). The MOSAs house the optical instruments responsible for the laser links between the spacecraft. A schematic of the spacecraft and the relevant subsystems can be found in Fig. 2. MOSA-1 is modeled to be linked to the platform via a rotational joint, MOSA-2 is fixed to the platform, and both test masses are free to move. During the acquisition sequence, DFACS is in charge of 16 degrees of freedom (DoF) per spacecraft: platform attitude (3 DoF), test mass position and attitude (6 DoF per test mass), and the angle control of MOSA-1 (1 DoF). The coordinate definition of each of the DoF can be found in Fig. 3.

Lower case letters are used for test mass relative displacement (x, y, z) and attitude (θ, η, ϕ) followed by subindices 1 and 2 for test mass 1 and 2, respectively. These coordinates represent displacement and attitude deviations with respect to a nominal position and attitude given by the respective MOSA housing. Capital letters are used for platform attitude (Θ, H, Φ) coordinates. The MOSA-1 relative attitude, defined as the angle between the nominal MOSA-1 attitude (30 degrees, distributed symmetrically to MOSA-2 along X axis as shown by the dark blue dotted lines) and the real MOSA-1 attitude (orange dotted line), is denoted by ϕ_{M1}. Finally, the platform position (X, Y, Z) is not controlled by DFACS.

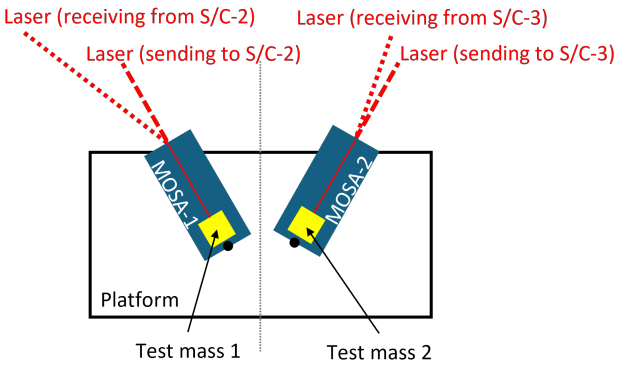

Fig. 2 LISA spacecraft schematic.

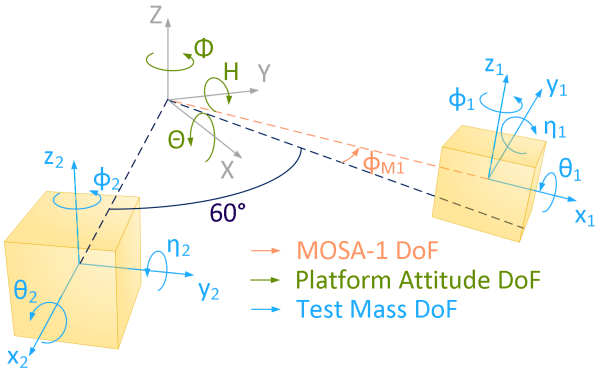

Fig. 3 DFACS degrees of freedom.

The guidance algorithm determines the reference trajectory which the spacecraft has to follow. The scanning is only performed by the platform and MOSA-1 (see Figure 4), and is based on an Archimedean spiral, in which the center is the position with the highest probability of finding the receiving spacecraft. This spiral is characterized by a constant tangential velocity and an exponential fade-in. During the scanning phase, the reference trajectory to be followed by the platform and MOSA-1 is defined as:

$$
\begin{aligned}
\Theta_{\text{ref}}(t) &= \frac{a}{l}\sqrt{bt}(1-e^{-\frac{t}{c}})\sin\left(\sqrt{bt}(1-e^{-\frac{t}{c}})\right) \\
H_{\text{ref}}(t) &= -\frac{1}{\sqrt{3}}\frac{a}{l}\sqrt{bt}(1-e^{-\frac{t}{c}})\sin\left(\sqrt{bt}(1-e^{-\frac{t}{c}})\right) \\
\Phi_{\text{ref}}(t) &= 0 \\
\phi_{M1,\text{ref}}(t) &= -\frac{a}{l}\sqrt{bt}(1-e^{-\frac{t}{c}})\cos\left(\sqrt{bt}(1-e^{-\frac{t}{c}})\right),
\end{aligned}
\tag{13}
$$

where

$$
a = \frac{kr_{\text{scan}}}{\pi}, \quad b = \frac{2\pi v_t}{kr_{\text{scan}}}, \tag{14}
$$

and l is the distance between the sending and receiving spacecraft, c is the fade-in time constant, k is the superimposition factor determining the degree of overlap between scanning cones, r_{scan} is the radius of the scanning cone at the receiving plane, and v_t is the constant tangential velocity. Table 1 contains the numerical values and Figure 4 shows the reference attitudes over a total scanning time of 2341 s, corresponding to a realistic LISA scenario. There is no reference for test mass position and attitude.

Table 1 Guidance parameters

Parameter	l	c	k	r_{scan}	v_t
Unit	m	-	-	m	rad m s^{-1}
Value	$2.5 \cdot 10^9$	1000	1	5337.5	2500

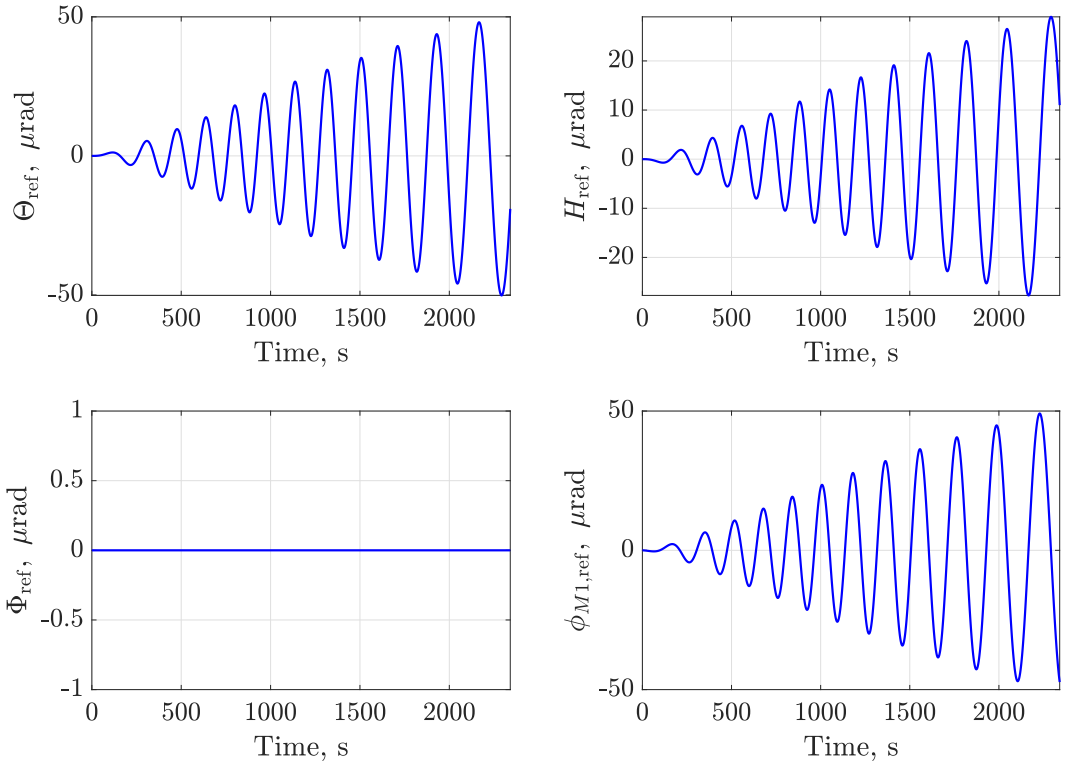

Fig. 4 Acquisition scanning pattern to be followed by the platform and MOSA-1.

The tracking error requirements on the platform and MOSA-1 attitude (Table 2) are expressed as Mean Performance Error (MPE). The MPE is defined as the time average for a time window Δt (7.3 s in DFACS), which corresponds to the expected value for that time window. For an error time signal $e(t)$, the MPE is mathematically defined as:

$$\bar{e}(t, \Delta t) = \langle e(t) \rangle_{\Delta t} = \frac{1}{\Delta t} \int_{t-\Delta t/2}^{t+\Delta t/2} e(\tau) d\tau. \tag{15}$$

Table 2 Platform and MOSA-1 performance requirements

Coordinate	Θ	H	$\Phi + \phi_{M1}$
Unit	µrad	µrad	µrad
σ_{MPE}	0.1	0.1	0.1

Although there are no explicit performance requirements on test masses during acquisition, closed-loop control shall respect the performance measurement limits. Therefore, the test mass deviations from its nominal position shall not exceed at any time during acquisition the performance limits shown in Table 3.

In summary, there are two types of requirements to be fulfilled during the acquisition scanning phase: mean performance error on platform and MOSA-1 tracking error, and maximum performance range on test mass coordinates.

Table 3 Test mass performance limits

Coordinate	x	y	z	θ	η	ϕ
Unit	µm	µm	µm	mrad	mrad	mrad
Value	100	100	150	5	9	9

B. DFACS Acquisition Mode Closed-loop Architecture

The model architecture describing the DFACS Acquisition Mode tracking problem is presented in Fig. 5, where r is the reference signal, $\ddot{r}$ is the acceleration reference signal, e_{ctrl} is the control error, u is the plant input, y is the plant output, e is the tracking error, and y_{meas} is the measured plant output. Moreover, G_{PLANT} is the plant model, Δ_{PLANT} captures the plant uncertainties, K is the controller model, G_{SENS} is the sensor dynamics model, G_{DEL} is the delay model, and F is the feedforward model.

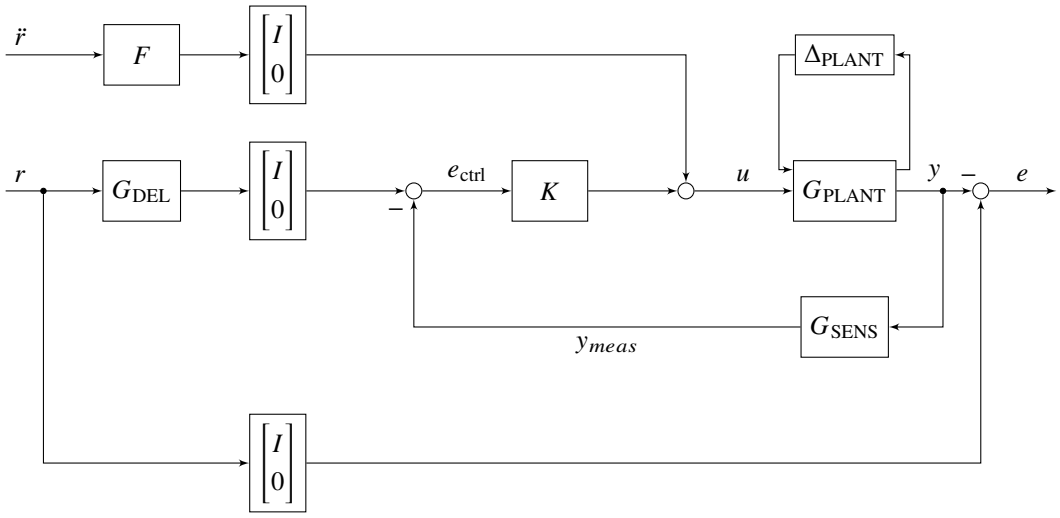

Fig. 5 Model architecture of DFACS Acquisition Mode.

The LISA multi-body system dynamics are represented through a linear, time-invariant model in G_{PLANT}. The output vector $y \in \mathbb{R}^{16\times 1}$ contains the 16 DFACS degrees of freedom:

$$y = \begin{bmatrix} \Theta & H & \Phi & x_1 & y_1 & z_1 & \theta_1 & \eta_1 & \phi_1 & x_2 & y_2 & z_2 & \theta_2 & \eta_2 & \phi_2 & \phi_{M1} \end{bmatrix}^{\top}. \tag{16}$$

The plant model describes the complete kinematic and dynamic coupling of all rigid bodies including the interaction of the different forces and torques and the actuator dynamics. The actuator dynamics impacting test mass and MOSA-1 coordinates are approximated as a two time step delay (implemented through a second-order Padé approximation), representing the actuator physical delay, and a commanding and communicating cycle delay. On the contrary, the platform actuator is approximated as a second-order response system, parameterised by its natural frequency and damping ratio followed by a one time step delay. In total, the plant model (G_{PLANT}) comprises 70 states.

Uncertainties in 25 plant model parameters are considered for the acquisition robustness analysis, which include mass and inertia properties for each of the bodies. These uncertainties are collected in Table 4 and represented in Fig. 5 by means of an LFT model whose uncertainty block $\Delta_{\text{PLANT}} \in \mathbb{R}^{62x62}$ captures the repetitions of the 25 uncertain parameters. Each parameter is distributed uniformly within the limits given in Table 4.

Table 4 Uncertain parameters

Name	Symbol	Nom. Value	Unit	Uncertainty	Repetitions
Platform mass	m_{PF}	1845.6	kg	±10%	3
Platform inertia	$I_{xx,\text{PF}}$	4454	kg m^2	±10%	1
	$I_{yy,\text{PF}}$	1012		±10%	1
	$I_{zz,\text{PF}}$	5073		±10%	1
	$I_{xy,\text{PF}}$	-42		±20%	2
	$I_{xz,\text{PF}}$	-10		±20%	2
	$I_{yz,\text{PF}}$	10		±20%	2
MOSA-1 mass	$m_{\text{MOSA}-1}$	162.7	kg	±10%	4
MOSA-1 inertia	$I_{xx,\text{MOSA}-1}$	6.8	kg m^2	±10%	1
	$I_{yy,\text{MOSA}-1}$	9.6		±10%	1
	$I_{zz,\text{MOSA}-1}$	9.6		±10%	2
	$I_{xy,\text{MOSA}-1}$	0.2		±20%	2
	$I_{xz,\text{MOSA}-1}$	1.1		±20%	2
	$I_{yz,\text{MOSA}-1}$	-0.1		±20%	2
MOSA-2 mass	$m_{\text{MOSA}-2}$	162.7	kg	±10%	3
MOSA-2 inertia	$I_{xx,\text{MOSA}-2}$	6.8	kg m^2	±10%	1
	$I_{yy,\text{MOSA}-2}$	9.6		±10%	1
	$I_{zz,\text{MOSA}-2}$	9.6		±10%	1
	$I_{xy,\text{MOSA}-2}$	0.2		±20%	2
	$I_{xz,\text{MOSA}-2}$	1.1		±20%	2
	$I_{yz,\text{MOSA}-2}$	-0.1		±20%	2
Test mass 1 mass	$m_{\text{TM}-1}$	1.9282	kg	±20%	6
Test mass 1 inertia	$I_{\text{TM}-1}$	$6.913 \cdot 10^{-4}$	kg m^2	±20%	6
Test mass 2 mass	$m_{\text{TM}-2}$	1.9282	kg	±20%	6
Test mass 2 inertia	$I_{\text{TM}-2}$	$6.913 \cdot 10^{-4}$	kg m^2	±20%	6

The DFACS controller design strategy is based on reducing the coupled multiple-input multiple-output (MIMO) plant system to a decoupled single-input single-output (SISO) one by applying a control input decoupling, which allows each input-output loop to be controlled by a SISO controller.

The platform and MOSA-1 attitude controllers were derived using the *systune* Matlab function. An eight- and sixth-order controller is synthesized for the platform and MOSA-1 coordinates, respectively. For each of the test mass coordinates, a third-order controller is used. Ultimately, the controller model K is a MIMO system (appending all 16 SISO controllers) formed by 66 states.

Sensor dynamics are approximated inside G_{SENS} through a two time step delay (sensor physical delay + measurement processing delay) for each of the 16 control loops, resulting in 32 additional states. The delay model G_{DEL} delays the reference attitudes r to ensure an optimal tracking in the nominal case, which adds additional 8 states (i.e., 2 states per delayed reference attitude).

In addition to the reference attitude r, a feedforward acceleration $\ddot{r}$ is implemented to ease the effort of the controller along the trajectory tracking. This feedforward acceleration is considered as an additional input to the system as shown in Fig. 5. The feedforward acceleration is also delayed such that, when propagated through the loop, it is synchronized with the reference signal r. This feedforward delay allows an optimal tracking in nominal conditions, and is implemented in F, comprising 9 states.

In summary, the DFACS Acquisition Mode model is composed of 8 inputs (i.e., reference trajectory r and feedforward acceleration $\ddot{r}$) and 16 outputs (i.e., e). Moreover, rearranging all the models of Fig. 5 into the augmented generalized plant results in a system of order 185 (i.e., 185 states).

IV. Probabilistic Robust Performance based on LFT and PCE

A. Methodology

The methodology employed to assess the impact of uncertainties over the LISA DFACS acquisition sequence is summarized in Algorithm 1. A LFT-based PCE is applied to the system described in Fig. 5 with the uncertainties in Table 4. The *Polynomial Chaos Expansion Toolbox* (PoCET) for MATLAB [35] is used to compute the LFT-based PCE projection integrals $\langle \cdot, \cdot \rangle$ of Eq. (11). This generates an expanded LFT system that needs to be simulated once to obtain the deterministic PCE coefficients. These coefficients can be used to reconstruct the PCE describing the probabilistic distribution of the DFACS performance. Sampling the uncertainty set and computing the pointing error via the PCE offers an efficient way of assessing the acquisition performance. This process is repeated N_{samples} times. The LFT-based PCE results will be compared to a classical Monte Carlo simulation campaign with the same number of simulations as PCE samples. The goal is to evaluate the accuracy and computational cost of this approach when the number of PCE samples is equivalent to that of MC samples.

B. Results

The acquisition verification results obtained using a LFT-based PCE are presented, based on a first order polynomial expansion ($d = 1$) and 20,000 samples. These results will be compared to those from a classical Monte Carlo campaign with 20,000 simulations.

First, the impact of the selected uncertainties on the platform and MOSA-1 relative attitude error is shown in Fig. 6. Compared to the nominal case (i.e., no uncertainties), the uncertainties significantly affect the attitude error throughout the scanning phase. This is specially noticeable in the platform Θ and H coordinates.

Algorithm 1 Probabilistic Robust Performance based on LFT and PCE

Inputs: reference trajectory [Eq. (13), Eq. (14) and Table 1], uncertain parameter definitions [Table 4], N_{samples}, d.
Build DFACS LFT based on Fig. 5, and Eq. (2) and Eq. (3).
Build expanded LFT-based PCE system [Eq. (10) and Eq. (11)].
Simulate expanded LFT-based PCE system [Eq. (10) and Eq. (11)] and obtain $Y(t)$.
Reconstruct output PCE: $y(t,\delta) \approx [I_{n_y} \bigotimes \Psi^{\top}(\delta)]Y(t)$.
for $i = 1 : N_{\text{samples}}$ **do**
    Sample uncertainty $\hat{\delta}_i$.
    Compute $\hat{y}_i(t,\hat{\delta}_i)$.
    if platform/MOSA-1 coordinate **then**
        Compute MPE of $\hat{y}_i(t,\hat{\delta}_i)$.
    else
        Compute $\max_t(\hat{y}_i(t,\hat{\delta}_i))$.
    end if
end for

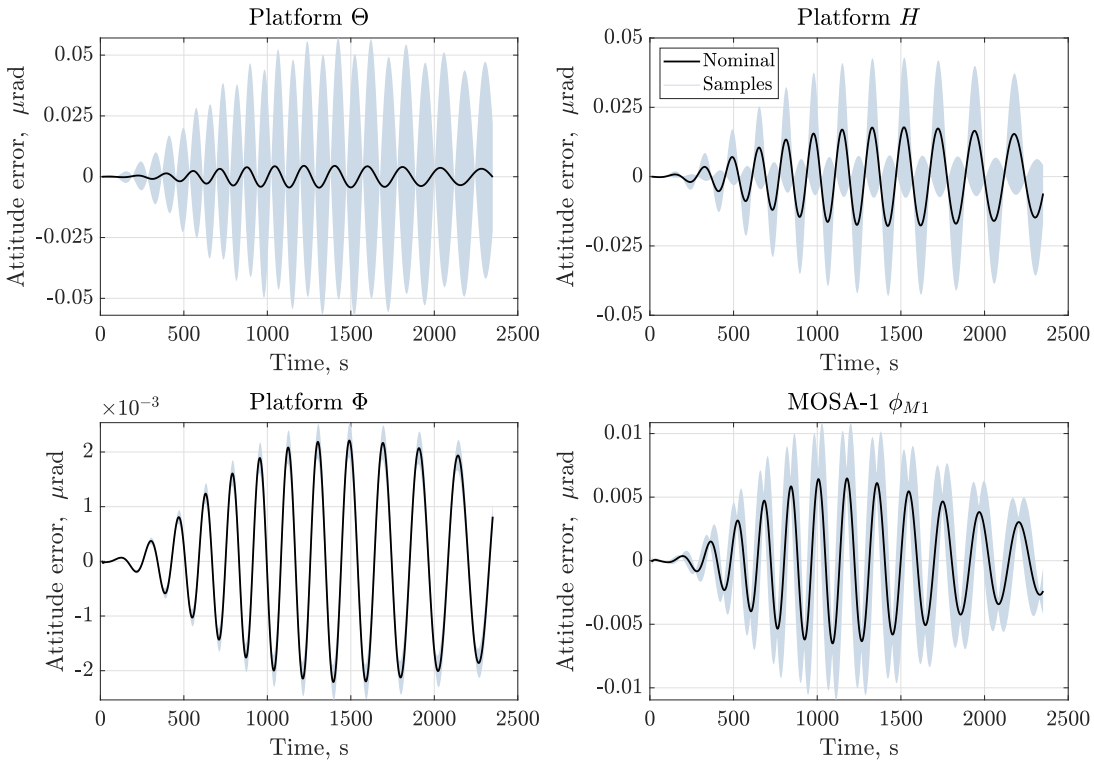

Fig. 6 Uncertainty impact on platform and MOSA-1 attitude error through PCE.

The MPE of each of the sampled trajectories is calculated in order to assess the performance against the requirements of Table 2. For brevity, only the MPE performance of the platform Θ coordinate is shown in Fig. 7, as it is the one that presents a larger variability. It can be seen that the system does not violate the requirement for any of the 20,000 PCE samples. Despite this, the mean or expected value of the performance is almost one order of magnitude larger than that of the nominal case. This highlights the influence of the uncertainties over the scanning tracking error. Table 5

collects the probabilistic distribution of the three platform and MOSA-1 performance axes by presenting their mean, standard deviation, and maximum value. No requirement violations are found and the performance remains well below the requirements.

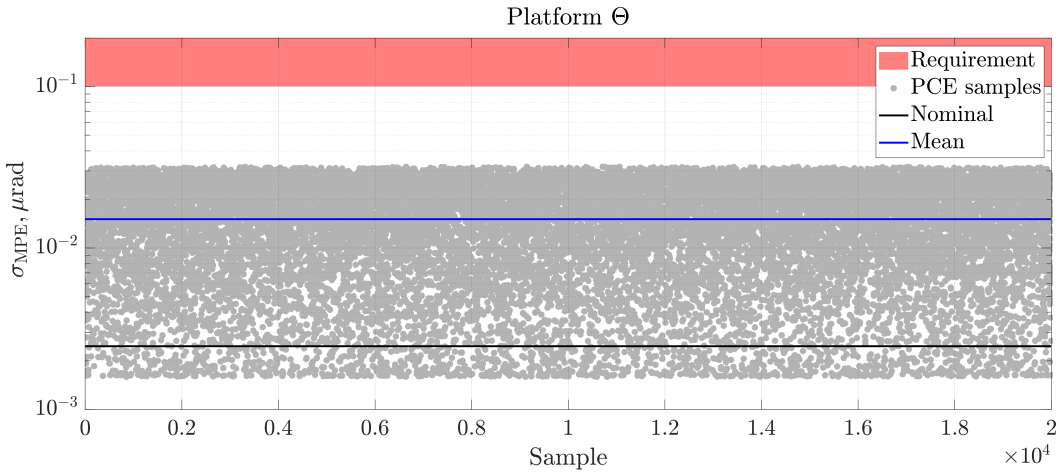

Fig. 7 Uncertainty impact on platform Θ MPE requirement through PCE.

Table 5 Probability distribution of platform and MOSA-1 performance

Coordinate	Θ	H	$\Phi + \phi_{M1}$
Unit	µrad	µrad	µrad
Mean	0.0151	0.0102	0.0035
Standard deviation	0.0085	0.0066	0.0006
Maximum	0.0319	0.0240	0.0059
Requirement	0.1	0.1	0.1

A similar analysis is performed on the test mass coordinates, which shall not exceed the values in Table 3. The influence of the uncertainties on test mass z_1 coordinate is presented in Fig. 8. The maximum deviation from its nominal position is ~ 1 µm, which is far away from the performance limit on test mass z coordinates (i.e., 150 µm). For completeness, the maximum deviation found after 20,000 PCE samples for each of the test mass coordinates is shown in Table 6.

Table 6 Verification of test mass performance

Coord.	x_1	y_1	z_1	θ_1	η_1	ϕ_1	x_2	y_2	z_2	θ_2	η_2	ϕ_2
Unit	µm	µm	µm	mrad	mrad	mrad	µm	µm	µm	mrad	mrad	mrad
Max.	0.019	0.089	1.028	0.004	0.009	0.008	0.078	0.059	2.043	0.011	0.003	0.0001
Req.	100	100	150	5	9	9	100	100	150	5	9	9

Results show that DFACS Acquisition Mode is robust against the considered uncertainties. All 15 performance requirements have been assessed through an LFT-based PCE approach and no violations have been detected. Moreover,

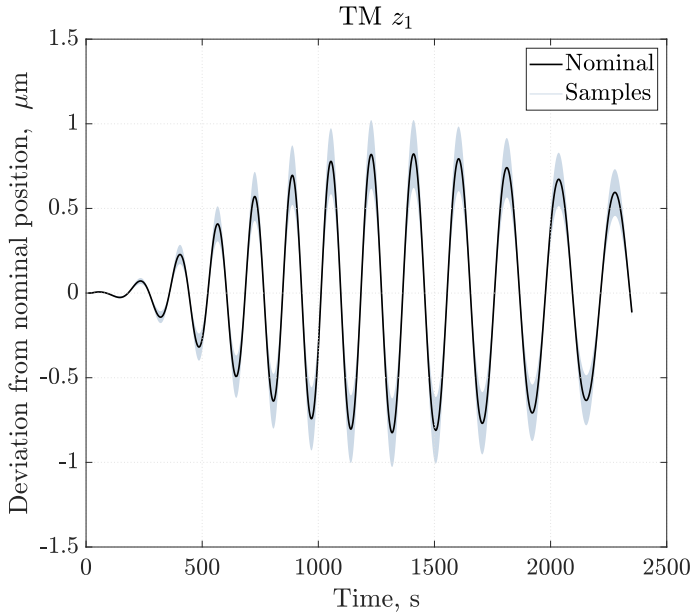

Fig. 8 Uncertainty impact on test mass z_1 deviation from nominal position through PCE.

the worst-case values obtained through sampling are all located far away from the requirements.

C. Comparison to Monte Carlo

A classical Monte Carlo campaign with 20,000 simulations is performed to assess the accuracy of the first-order LFT-based PCE representation and the computational time needed to carry out the analysis. For that, the Monte Carlo and PCE probabilistic distributions are compared using their mean, standard deviation, histograms, and cumulative probability functions. The comparison for the platform Θ coordinate is shown here. The same exercise can be carried out for the remaining coordinates.

The mean and standard deviation comparison for the MPE performance requirement on platform Θ can be found in Table 7. The first-order PCE is able to obtain an excellent approximation of the Monte Carlo distribution metrics (i.e., relative difference of 0.004% for mean and 0.01% for standard deviation), what is a good indicator of the accuracy of the PCE. In addition, the histograms and cumulative probability functions in Fig. 9 are used to visualize the closeness between the MC and PCE distributions. It is demonstrated that PCE can accurately approximate the results from the MC simulation, as illustrated by the near-perfect overlap of their histograms and cumulative distributions. PCE can then be used as an alternative to Monte Carlo to assess various probabilities.

The main benefit of using the LFT-based PCE approach relies in the computational time required to perform the verification. Monte Carlo samples the uncertainty space and simulates the model in Fig.5 20,000 times for different uncertainty combinations. The approach described in Algorithm 1 builds a surrogate model with a polynomial form, which is much faster to evaluate than the original model. This method replaces the time-consuming simulations (i.e.,

Table 7 Mean and standard deviation comparison of MC vs PCE

Method	MC	PCE ($d = 1$)	Rel. difference
Unit	µrad	µrad	%
Mean	0.0150842	0.0150848	0.004
Standard deviation	0.008534	0.008533	0.01

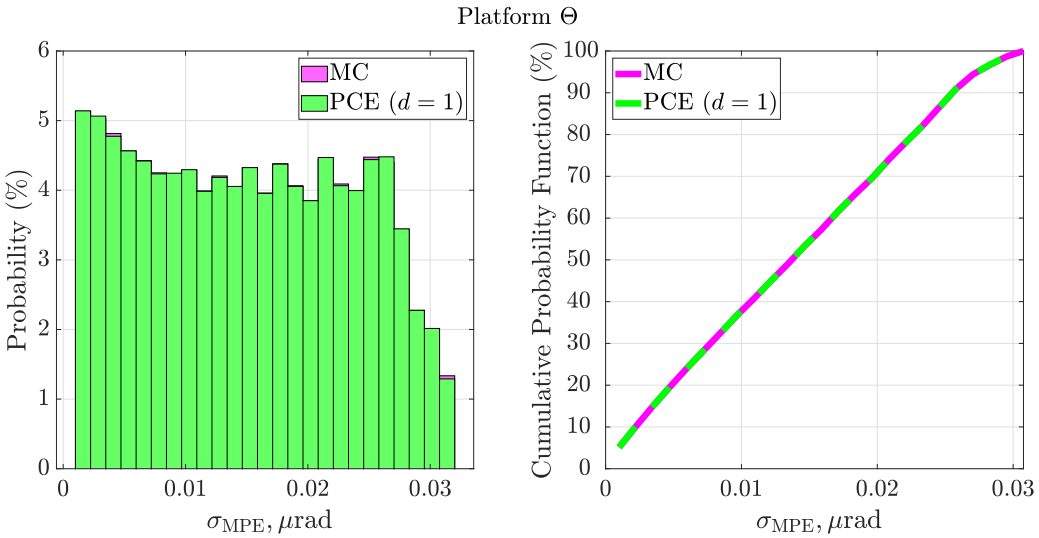

Fig. 9 Histogram and cumulative probability function comparison of MC and PCE verification results.

Monte Carlo) with the direct input of uncertainties into a polynomial that outputs the system's response. The surrogate PCE model is evaluated 20,000 times using various uncertainty realizations. Although building/obtaining the surrogate model (i.e., first four steps in Algorithm 1) results in additional computational cost, this investment is justified by the reduction in evaluation time of the surrogate model compared to the original model. Table 8 collects the computational time difference. The DFACS acquisition verification process is almost six times faster using Algorithm 1 compared to Monte Carlo. Additionally, the accuracy is not compromised, as the results from both verifications are nearly identical (i.e., as seen in Table 7 and Fig. 9).

Table 8 Computational time comparison of MC vs PCE

Method	MC	PCE ($d = 1$)
Build time	-	210 s (~ 3 min)
Sample time	8389.8 s (~ 2.3 h)	1238.9 s (~ 21 min)
Total time	8389.8 s (~ 2.3 h)	1448.9 s (~ 24 min)

The DFACS tracking problem scenario is efficiently verified for all DoF using Algorithm 1 and no performance requirements are violated. The results after 20,000 samples/simulations show an excellent agreement with Monte Carlo, but are obtained in a fraction of the time.

V. Conclusion

The LISA DFACS Acquisition Mode performance has been efficiently verified in this paper through an approach based on linear fractional transformation and polynomial chaos expansion. Although this method offers promising computational benefits in simpler models, some of the recently developed V&V approaches do not scale well with the model size, what prevents them from being used in the verification and validation processes in industry. This paper shows how Algorithm 1 offers an alternative verification of a high-fidelity DFACS benchmark derived from a challenging real-world mission such as the LISA mission. This alternative verification approach has been successfully applied to the DFACS Acquisition Mode model composed of 8 inputs, 16 outputs, and 185 states, with 25 parametric uncertainties. This promises a better scalability than classical robustness methods like μ-analysis or integral quadratic constraints. The LFT-based PCE approach has reduced the verification time from approximately 2.3 h to roughly 24 min. In addition, nearly identical results to those achieved via Monte Carlo are obtained. This paper has demonstrated the usefulness of this alternative approach in a real-world scenario, highlighting its potential to be used in industry.

Acknowledgments

The authors would like to thank Ralf Schubert and Luca Evangelisti from Airbus Defence and Space GmbH for their valuable support, guidance, and feedback.

References

[1] Houba, N., Delchambre, S., Ziegler, T., and Fichter, W., "Optimal Estimation of Tilt-to-Length Noise for Spaceborne Gravitational-Wave Observatories," *Journal of Guidance, Control, and Dynamics*, Vol. 45, No. 6, 2022, pp. 1078–1092. https://doi.org/10.2514/1.G006064.

[2] Joffre, E., Wealthy, D., Fernandez, I., Trenkel, C., Voigt, P., Ziegler, T., and Martens, W., "LISA: Heliocentric formation design for the laser interferometer space antenna mission," *Advances in Space Research*, Vol. 67, No. 11, 2021, pp. 3868–3879. https://doi.org/10.1016/j.asr.2020.09.034.

[3] Schleicher, A., Ziegler, T., Schubert, R., Brandt, N., Bergner, P., Johann, U., Fichter, W., and Grzymisch, J., "In-orbit performance of the LISA Pathfinder drag-free and attitude control system," *CEAS Space Journal*, Vol. 10, 2018, pp. 471–485. https://doi.org/10.1007/s12567-018-0204-x.

[4] Vidano, S., Novara, C., Colangelo, L., and Grzymisch, J., "The LISA DFACS: a Nonlinear Model for the Spacecraft Dynamics," *Aerospace Science and Technology*, Vol. 107, 2020, p. 106313. https://doi.org/10.1016/j.ast.2020.106313.

[5] Hechenblaikner, G., Delchambre, S., and Ziegler, T., "Optical link acquisition for the LISA mission with in-field pointing architecture," *Optics & Laser Technology*, Vol. 161, 2023, p. 109213. https://doi.org/10.1016/j.optlastec.2023.109213.

[6] Izquierdo Serra, M., Martin, M., Delchambre, S., Winkler, S., and Pfifer, H., "Probabilistic Verification of Spacecraft

Acquisition Sequence using Polynomial Chaos Expansion," *AIAA SCITECH 2025 Forum*, Orlando, FL, USA, 2025. https://doi.org/10.2514/6.2025-0315.

[7] Marcos, A., Roux, C., Rotunno, M., Joos, H.-D., Bennani, S., Peñín, L. F., and Caramagno, A., "The V&V Problematic for Launchers: Current Practice and Potential Advantages on the Application of Modern Analysis Techniques," *ESA Guidance, Navigation and Control Conference*, Karlovy Vary, Czech Republic, 2011.

[8] Dennehy, C., Bennani, S., Shankar, U., Vandersteen, J., VanZwieten, T., Von der Porten, P., Wolf, A., Girouart, B., and Casasco, M., "Verification and Validation (V&V) of Guidance & Control Systems: Results from the First Inter-Agency Workshop on GNC V&V," *Proceedings of the 44th Annual American Astronautical Society Guidance, Navigation, and Control Conference, 2022*, Springer International Publishing, Breckenridge, CO, USA, 2024, pp. 399–432. https://doi.org/10.1007/978-3-031-51928-4_25.

[9] Helton, J. C., Johnson, J. D., Sallaberry, C. J., and Storlie, C. B., "Survey of Sampling-Based Methods for Uncertainty and Sensitivity Analysis," *Reliability Engineering & System Safety*, Vol. 91, No. 10-11, 2006, pp. 1175–1209. https://doi.org/10.1016/j.ress.2005.11.017.

[10] Hanson, J. M., and Beard, B. B., "Applying Monte Carlo Simulation to Launch Vehicle Design and Requirements Verification," *Journal of Spacecraft and Rockets*, Vol. 49, No. 1, 2012, pp. 136–144. https://doi.org/10.2514/1.52910.

[11] Hanson, J., and Hall, C., "Learning About Ares I from Monte Carlo Simulation," *AIAA Guidance, Navigation and Control Conference and Exhibit*, AIAA, 2008, p. 6622. https://doi.org/10.2514/6.2008-6622.

[12] Young, P. M., Newlin, M. P., and Doyle, J. C., "μ Analysis with Real Parametric Uncertainty," *Proceedings of the 30th IEEE Conference on Decision and Control*, IEEE, 1991, pp. 1251–1256. https://doi.org/10.1109/CDC.1991.261579.

[13] Ferreres, G., *A Practical Approach to Robustness Analysis with Aeronautical Applications*, Springer, New York, 1999. https://doi.org/10.1007/b116799.

[14] Roos, C., Lescher, F., Biannic, J.-M., Döll, C., and Ferreres, G., "A set of μ-analysis based tools to evaluate the robustness properties of high-dimensional uncertain systems," *Proceedings of the IEEE International Symposium on Computer-Aided Control System Design*, IEEE, Denver, CO, USA, 2011, pp. 644–649. https://doi.org/10.1109/CACSD.2011.6044547.

[15] Megretski, A., and Rantzer, A., "System Analysis via Integral Quadratic Constraints," *IEEE Transactions on Automatic Control*, Vol. 42, No. 6, 1997, pp. 819–830. https://doi.org/10.1109/9.587335.

[16] Veenman, J., Scherer, C. W., and Köroglua, H., "Robust stability and performance analysis with integral quadratic constraints," *European Journal of Control*, Vol. 31, 2016, pp. 1–32. https://doi.org/10.1016/j.ejcon.2016.04.004.

[17] Biertümpfel, F., Pholdee, N., Bennani, S., and Pfifer, H., "Finite Horizon Worst Case Analysis of Linear Time-Varying Systems Applied to Launch Vehicle," *IEEE Transactions on Control Systems Technology*, Vol. 31, No. 6, 2023, pp. 2393–2404. https://doi.org/10.1109/TCST.2023.3260728.

[18] Biertümpfel, F., and Pfifer, H., "Finite Horizon Analysis of Autolanded Aircraft in Final Approach under Crosswind," *Control Engineering Practice*, Vol. 122, 2022, p. 105105. https://doi.org/10.1016/j.conengprac.2022.105105.

[19] Biertümpfel, F., Bennani, S., and Pfifer, H., "Time-Varying Robustness Analysis of Launch Vehicles Under Thrust Perturbations," *Advanced Control for Applications: Engineering and Industrial Systems*, Vol. 3, No. 4, 2021, p. e93. https://doi.org/10.1002/adc2.93.

[20] Biannic, J.-M., Roos, C., Bennani, S., Boquet, F., Preda, V., and Girouart, B., "Advanced probabilistic μ-analysis techniques for AOCS validation," *European Journal of Control*, Vol. 62, 2021, pp. 120–129. https://doi.org/10.1016/j.ejcon.2021.06.019.

[21] Evangelisti, L. L., "Probabilistic Robustness Analysis with Aerospace Applications," Ph.D. thesis, Technische Universität Dresden, 2023.

[22] Sullivan, T. J., *Introduction to Uncertainty Quantification*, Vol. 63, Springer, 2015. https://doi.org/10.1007/978-3-319-23395-6.

[23] Ghanem, R., Higdon, D., and Owhadi, H., *Handbook of Uncertainty Quantification*, Vol. 6, Springer, 2017. https://doi.org/10.1007/978-3-319-12385-1.

[24] Wiener, N., "The Homogeneous Chaos," *American Journal of Mathematics*, Vol. 60, No. 4, 1938, pp. 897–936. https://doi.org/10.2307/2371268.

[25] Ghanem, R. G., and Spanos, P. D., *Stochastic Finite Elements: a Spectral Approach*, Springer, 1991. https://doi.org/10.1007/978-1-4612-3094-6.

[26] Xiu, D., and Karniadakis, G. E., "The Wiener–Askey Polynomial Chaos for Stochastic Differential Equations," *SIAM Journal on Scientific Computing*, Vol. 24, No. 2, 2002, pp. 619–644. https://doi.org/10.1137/S1064827501387826.

[27] Xiu, D., and Karniadakis, G. E., "Modeling uncertainty in flow simulations via generalized polynomial chaos," *Journal of Computational Physics*, Vol. 187, No. 1, 2003, pp. 137–167. https://doi.org/10.1016/S0021-9991(03)00092-5.

[28] Evangelisti, L. L., and Pfifer, H., "On the application of Galerkin projection based polynomial chaos in linear systems and control," *Automatica*, Vol. 167, 2024, p. 111768. https://doi.org/10.1016/j.automatica.2024.111768.

[29] Evangelisti, L. L., and Pfifer, H., "Probabilistic Robustness Analysis of Uncertain LTV systems in Linear Fractional Representation," *IEEE Control Systems Letters*, Vol. 6, 2021, pp. 428–433. https://doi.org/10.1109/LCSYS.2021.3078881.

[30] Evangelisti, L. L., and Pfifer, H., "Finite-Horizon Robustness Analysis of an Automatic Landing System Under Probabilistic Uncertainty," *Journal of Guidance, Control, and Dynamics*, Vol. 47, No. 3, 2024, pp. 464–472. https://doi.org/10.2514/1.G007518.

[31] Hecker, S., "Generation of low order LFT Representations for Robust Control Applications," Ph.D. thesis, Technische Universität München, 2006.

[32] Piprek, P., "Robust Trajectory Optimization Applying Chance Constraints and Generalized Polynomial Chaos," Ph.D. thesis, Technische Universität München, 2020. https://doi.org/10.13140/RG.2.2.17878.88649.

[33] Marelli, S., and Sudret, B., "UQLab User Manual–Polynomial Chaos Expansions," Tech. rep., Chair of Risk, Safety & Uncertainty Quantification, ETH Zurich, 2015. https://doi.org/10.13140/RG.2.1.3778.7366, report UQLab-V0.9-104.

[34] Blatman, G., and Sudret, B., "Anisotropic parcimonious polynomial chaos expansions based on the sparsity-of-effects principle," *10th International Conference in Structural Safety and Relability (ICOSSAR'09)*, Osaka, Japan, 2009.

[35] Petzke, F., Mesbah, A., and Streif, S., "PoCET: a Polynomial Chaos Expansion Toolbox for Matlab," *21st IFAC World Congress 2020*, Berlin, Germany, 2020. https://doi.org/10.1016/j.ifacol.2020.12.560.